Near-Surface Frontogenesis and Atmospheric Instability along the U.S. East Coast during the Extratropical Transition of Hurricane Matthew (2016)

SCOTT W. POWELL

Department of Meteorology, Naval Postgraduate School, Monterey, California

MICHAEL M. BELL

Department of Atmospheric Science, Colorado State University, Fort Collins, Colorado

ABSTRACT

Hurricane Matthew locally generated more than 400 mm of rainfall on 8–9 October 2016 over the eastern Carolinas and Virginia as it transitioned into an extratropical cyclone. The heaviest precipitation occurred along a swath situated up to 100–200 km inland from the coast and collocated with enhanced low-tropospheric frontogenesis. Analyses from version 3 of the Rapid Refresh (RAPv3) model indicate that rapid frontogenesis occurred over eastern North and South Carolina and Virginia on 8 October, largely over a 12-h time period between 1200 UTC 8 October and 0000 UTC 9 October. The heaviest rainfall in Matthew occurred when and where spiral rainbands intersected the near-surface front, which promoted the lift of conditionally unstable, moist air. Parallel to the spiral rainbands, conditionally unstable low-tropospheric warm, moist oceanic air was advected inland, and the instability was apparently released as the warm air mass rose over the front. Precipitation in the spiral rainbands intensified on 9 October as the temperature gradient along the near-surface front rapidly increased. Unlike in Hurricane Floyd over the mid-Atlantic states, rainfall totals within the spiral rainbands of Matthew as they approached the near-surface front evidently were not enhanced by release of conditional symmetric instability. However, conditional symmetric instability release in the midtroposphere may have enhanced rainfall 200 km northwest of the near-surface front. Finally, although weak cold-air damming occurred prior to heavy rainfall, damming dissipated prior to frontogenesis and did not impact rainfall totals.

1. Introduction

Inland flooding caused by heavy rainfall frequently inflicts property damage and human casualties in the United States during landfalling tropical cyclones. Over the past several decades, model prediction of extreme rainfall associated with tropical cyclones has improved, but precisely forecasting the locations of heaviest rainfall remains challenging. Hurricane Matthew (2016) was one recent example of an extreme rainfall event over the U.S. East Coast associated with a tropical cyclone. A total of 24 people died in North Carolina (NC) and South Carolina (SC) as a result of freshwater flooding during Matthew (Stewart 2017). Matthew tracked northward out of the Caribbean Sea and closely paralleled the southeastern U.S. coast from 7 to 9 October 2016. It briefly made landfall in northeastern SC on 8 October as a tropical

cyclone undergoing extratropical transition (Jones et al. 2003; Evans et al. 2017). The center then moved northeastward along the coast of the Carolinas while the heaviest rainfall associated with the cyclone persisted 100–200 km inland (Stewart 2017). The storm was declared post-tropical operationally at 0900 UTC 9 October. Figure 1 illustrates the best track and minimum pressure for Matthew.

Over 400 mm (~15.75 in.) of rain fell over parts of eastern SC, NC, and Virginia (VA) during a 24-h-long period on 8–9 October, and over 100 mm of precipitation occurred over a much broader region within each state (Stewart 2017). As a result, significant flooding occurred during and days after the storm along North Carolinian rivers. The flooding was preceded by a rainy September, which included up to about 250 mm (~10 in.) of precipitation that occurred during the passage of Tropical Storm Hermine on 1–2 September. The largest rain totals were focused along a path near where

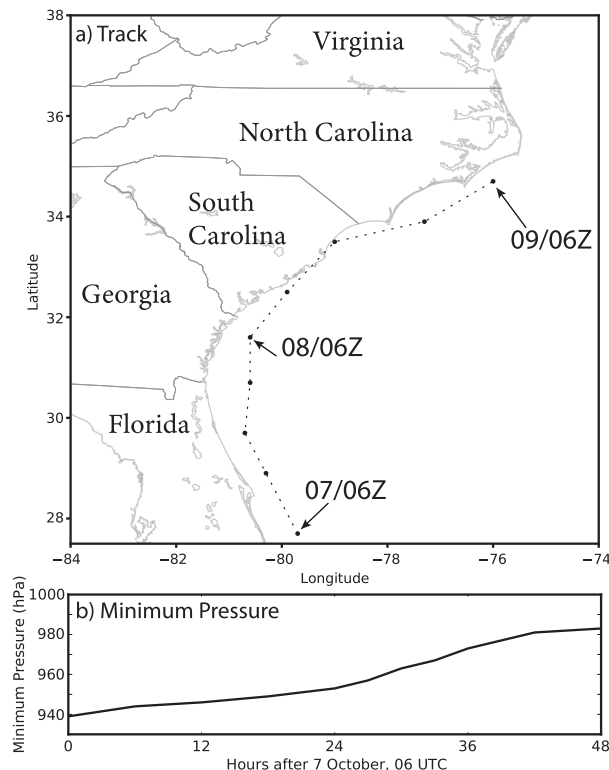*Corresponding author*: Scott W. Powell, scott.powell@nps.edu

FIG. 1. (a) Track of Hurricane Matthew in the National Hurricane Center best track. Dots represent a new position every 6 h, and position at 0600 UTC 7–9 Oct is denoted with arrows. (b) Estimated minimum surface pressure of Hurricane Matthew in the best track.

the National Weather Service identified a "quasi-stationary coastal front" in operational analysis (NOAA 2018a).

In terms of extreme precipitation that occurred, particularly over NC, the closest recorded analog to Matthew is perhaps Hurricane Floyd, which directly impacted NC on 15–16 September 1999 before transitioning into an extratropical cyclone and exhibiting a similar west-of-track maximum in precipitation that caused extensive flooding along a large swath of the U.S. East Coast. Atallah and Bosart (2003) explored the spatial precipitation distribution during Floyd in detail with particular emphasis on the synoptic-scale forcing that led to the extreme rainfall. They found that extreme precipitation coincided with strong isentropic ascent occurring along a deep coastal baroclinic zone between a cold core potential vorticity (PV) anomaly associated with an approaching midlatitude trough and the warm core PV anomaly associated with Floyd. Within an environment supportive of synoptic-scale ascent, the baroclinic zone appeared to focus the most intense precipitation along a convergence boundary near a surface front. When examining 32 tropical cyclones that made landfall along the U.S. East Coast between 1950 and 1998, Atallah et al. (2007) reached similar conclusions about the synoptic-scale forcing common to extreme rain

events in tropical cyclones. They found also that left-of-track precipitation distributions like those experienced during Matthew occur frequently when a tropical cyclone interacts strongly with a midlatitude trough located within 1500 km to the northwest, and that positively tilted troughs are ideal for extension of a baroclinic zone from the west to north quadrants of a transitioning cyclone.

In a modeling study of the extratropical transition of Floyd, Colle (2003) found that "strong frontogenesis as well as moist symmetric instability below 800 mb and neutrality aloft resulted in a narrow and intense band of precipitation just inland of the coast" (p. 2924). Consistent with Atallah and Bosart (2003), he found that diabatic heating helped drive frontogenesis because the greatest latent heat release at midlevels occurred on the warm side of the developing front. The extensive flooding during Floyd was not well predicted, and this was ultimately attributed to the combination of processes involved in forcing the band of heavy precipitation, and in particular, the failure of models to properly represent latent heating. In contrast, the threat of large inland precipitation amounts was better predicted in advance of Matthew. Over 24 h in advance, between 203 mm (8 in.) and 305 mm (12 in.) of rainfall, with local amounts over 381 mm (15 in.), were predicted for a swath in eastern NC closely matching the eventual location of the precipitation (NOAA 2018b). Nonetheless, the banded precipitation pattern ultimately observed (section 3) was not explicitly predicted, and rainfall in northeastern NC and southeastern VA was consistently underpredicted on 7–8 October prior to the onset of precipitation there.

Although our understanding of synoptic-scale processes that support development of swaths of heavy rainfall during events such as Floyd or Matthew has improved, questions remain about regional-scale and mesoscale processes that might impact the location and intensity of rainfall. For example, Bosart and Dean (1991) and Atallah and Bosart (2003) suggested that cold-air damming east of the Appalachian Mountains accompanies heavy precipitation as a cyclone undergoes extratropical transition. They did not quantify the potential effect of cold-air damming on precipitation, but they acknowledged that it was of secondary importance to other processes that encourage intense rainfall accompanying a cyclone undergoing extratropical transition. Damming is common when surface pressures are higher over New England than over the southeastern United States. The pressure gradient force moves air southward parallel to the Appalachians, and the cool low-level air becomes trapped on the east side of the mountains (Bell and Bosart 1988). Meanwhile, as a tropical cyclone approaches the East Coast, it advects

warm, moist air inland around its northeastern quadrant. Where it meets cooler, drier air over land, a coastal front develops; the temperature gradient along such a front could be enhanced if accompanied by cold-air damming (Croke 2005). Atallah et al. (2007) noted that left-of-track precipitation distributions can occur without cold-air damming, even though such distributions are common in particular for tropical cyclones moving up the East Coast where cold-air damming might occur. Colle (2003) claimed that terrain did not affect the precipitation distribution in Floyd; however, his model simulations were focused farther north from New Jersey to Connecticut, where the mountains are shorter and closer to the coast than in the Carolinas and Virginia. Also, Garcia-Rivera et al. (2016) concluded that the Appalachian Mountains and cold-air damming did not impact precipitation during a much weaker Tropical Storm Kyle over NC in 2002.

As Matthew moved northward along the U.S. East Coast, radar data, which will be analyzed later in this article (section 4), indicated that the most intense rainfall at a given time was confined to narrow regions along the inland portions of spiral rainbands rotating around the cyclone. The study of Colle (2003) discussed the importance of frontogenesis, moisture advection and convergence, and release of conditional symmetric instability in supporting extremely intense rainfall. This study investigates in what ways the combined effects of cold-air damming, frontogenesis, moisture convergence, and atmospheric instability influenced the production of large rainfall totals during Hurricane Matthew. Specifically, we will address the following questions:

1) Could cold-air damming induced by the Appalachian Mountains, which were approximately 300 km away from the locations of the largest rainfall totals in Matthew, have enhanced rainfall in eastern SC, NC, and VA (section 3)?
2) What was the spatial distribution of frontogenesis over eastern NC on 8 October (section 4)?
3) Did conditional symmetric instability enhance rainfall during Matthew (section 5)?

First, we will briefly demonstrate that synoptic-scale conditions were consistent with those associated with left-of-track precipitation maxima described by Atallah et al. (2007).

2. Operational analysis and data

To characterize the synoptic-scale environment in place during Matthew (section 3), we used hourly analysis from version 3 of the operational Rapid Refresh (RAPv3; Benjamin et al. 2016) model. RAPv3 has approximately 13-km horizontal grid spacing and 51 vertical levels with a model top at 10 hPa. The analysis used herein has vertical grid spacing of 25 hPa. It assimilates a variety of ground-based, satellite-based, aircraft, and rawinsonde observations to generate its analyses, including observations of radar reflectivity and Doppler velocity from the Weather Surveillance Radar-1988 Doppler (WSR-88D) network. Some reflectivity observations from WSR-88D are shown in section 4. Specifically, data from radars serving the Columbia, SC (KCAE); Charleston, SC (KCLX); Wilmington, NC (KLTX); Raleigh, NC (KRAX); Newport/Morehead City, NC (KMHX); Blacksburg, VA (KFCX); and Wakefield, VA (KAKQ) forecast offices were used. The radar data were interpolated to a rectilinear grid with horizontal grid spacing of 1 km and vertical grid spacing of 500 m.

Surface station data were also utilized to determine whether and when cold-air damming occurred in SC, NC, or VA. An objective algorithm for cold-air damming detection, which is described by Bailey et al. (2003), was applied to mean sea level pressure estimates over the Carolinas and Virginia. The stations used by this algorithm are mapped in Fig. 2; the results are discussed in section 3.

3. Synoptic-scale environment and rainfall observations

Figure 3 shows the evolution of 500-hPa geopotential height (black contours in decameters) on 7–9 October. At 0000 UTC 7 October[1] (Fig. 3a), a long-wave trough axis was present west of 100°W while Matthew was centered off the south Florida coast. By 0000 UTC 8 October (Fig. 3c), the long-wave trough axis was located between 90° and 95°W. During the earlier half of 8 October (Figs. 3c,d), the midlatitude long-wave trough moving eastward across the United States temporarily became more negatively tilted. However, as Matthew moved offshore North Carolina, the trough developed a positive tilt (Fig. 3e). As mentioned in section 1, the positive tilt is favorable for the formation of a baroclinic zone to the north of the cyclone. Gray contours in Fig. 3 depict mean sea level pressure (MSLP) in hPa. At 0000 UTC 7 October, an eastward-moving surface high pressure was located near 45°N, 75°W, so that the pressure gradient along the U.S. East Coast was generally oriented from northeast to southwest on 7–9 October, a prerequisite for cold-air damming. From 0000 UTC 7 October (Fig. 3a) to 0000 UTC 8 October (Fig. 3c), a

---

[1] In figures, the convention XX/YY UTC in which XX = day of month and YY = hour will be used to denote dates and times.
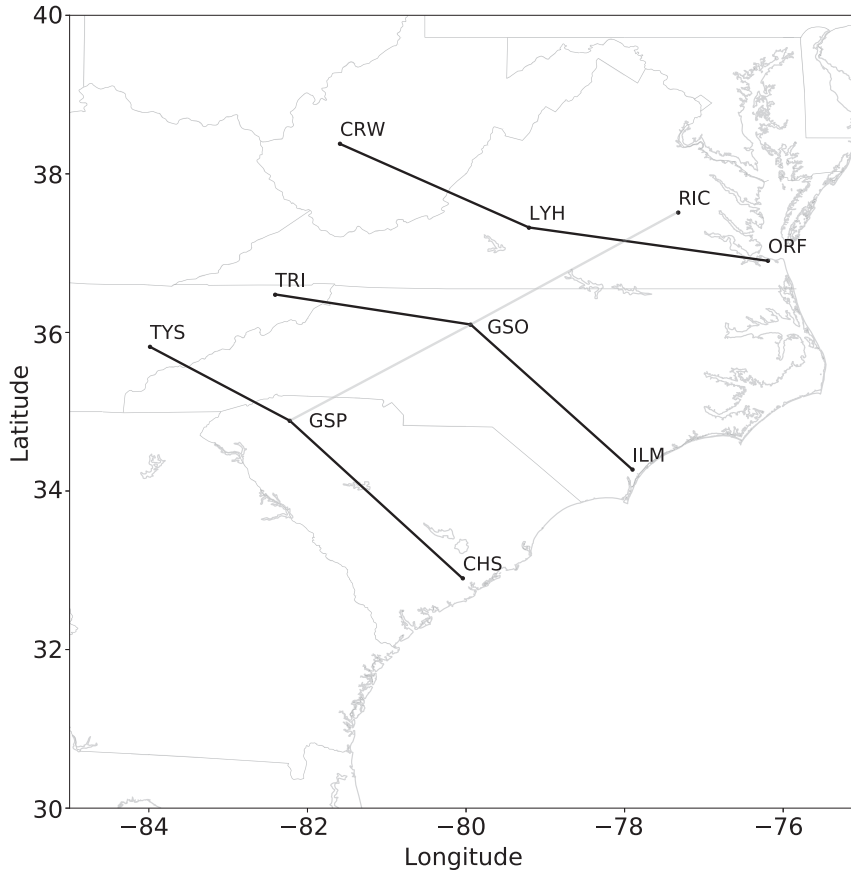
FIG. 2. Outline of surface weather stations used in cold-air damming detection algorithm. Figure is a recreation of Fig. 3 from Bailey et al. (2003).

weakening surface pressure ridge was present east of the Appalachians.

Figure 4 includes three quantities computed from RAP at 950 hPa: frontogenesis (K $100 \, \text{km}^{-1}$ $3 \, \text{h}^{-1}$; shading), potential temperature θ (K; black lines), and horizontal wind (m s^{-1}; vectors) analyzed by RAP every 6 h from 0000 UTC 7 October to 0000 UTC 9 October. The black dashed line represents the 298-K θ contour, and the θ contour interval is 2 K. Frontogenesis F is a diagnostic quantity defined as the Lagrangian derivative of the horizontal temperature (T) gradient:

$$F = \frac{d}{dt} |\nabla_h \theta| \qquad (1)$$

in which

$$\frac{d}{dt} = \frac{\partial}{\partial t} + u \frac{\partial}{\partial x} + v \frac{\partial}{\partial y} + w \frac{\partial}{\partial z},$$

and u, v, and w represent, respectively, zonal, meridional, and vertical wind; and the subscript h refers to a horizontal gradient. In this article, F is approximated by

the Petterssen frontogenesis (Petterssen 1936). It includes the effects of deformation and divergence on formation/destruction of temperature gradients:

$$F \approx -\frac{1}{|\nabla_h \theta|} \left\{ \left[\left(\frac{\partial \theta}{\partial x} \right)^2 \frac{\partial u}{\partial x} + \left(\frac{\partial \theta}{\partial y} \right)^2 \frac{\partial v}{\partial y} \right] + \left[\frac{\partial \theta}{\partial x} \frac{\partial \theta}{\partial y} \left(\frac{\partial v}{\partial x} + \frac{\partial u}{\partial y} \right) \right] \right\}. \qquad (2)$$

Partial derivatives in Eq. (2) were computed using first-ordered centered differencing in space. Convergence of θ gradients played a negligible role in frontogenesis (not shown).

Early on 7 October, a wedge of cool ($\theta = 294$–296 K) air located inland over SC and NC moved westward toward the mountains (Figs. 4a–c). As Matthew approached on 8 October, the cool air moved back toward the east as it simultaneously wrapped around the western and southern sides of the cyclone. The temperature field and ridge east of the mountains suggest that at least weak cold-air damming took place during 7–8 October
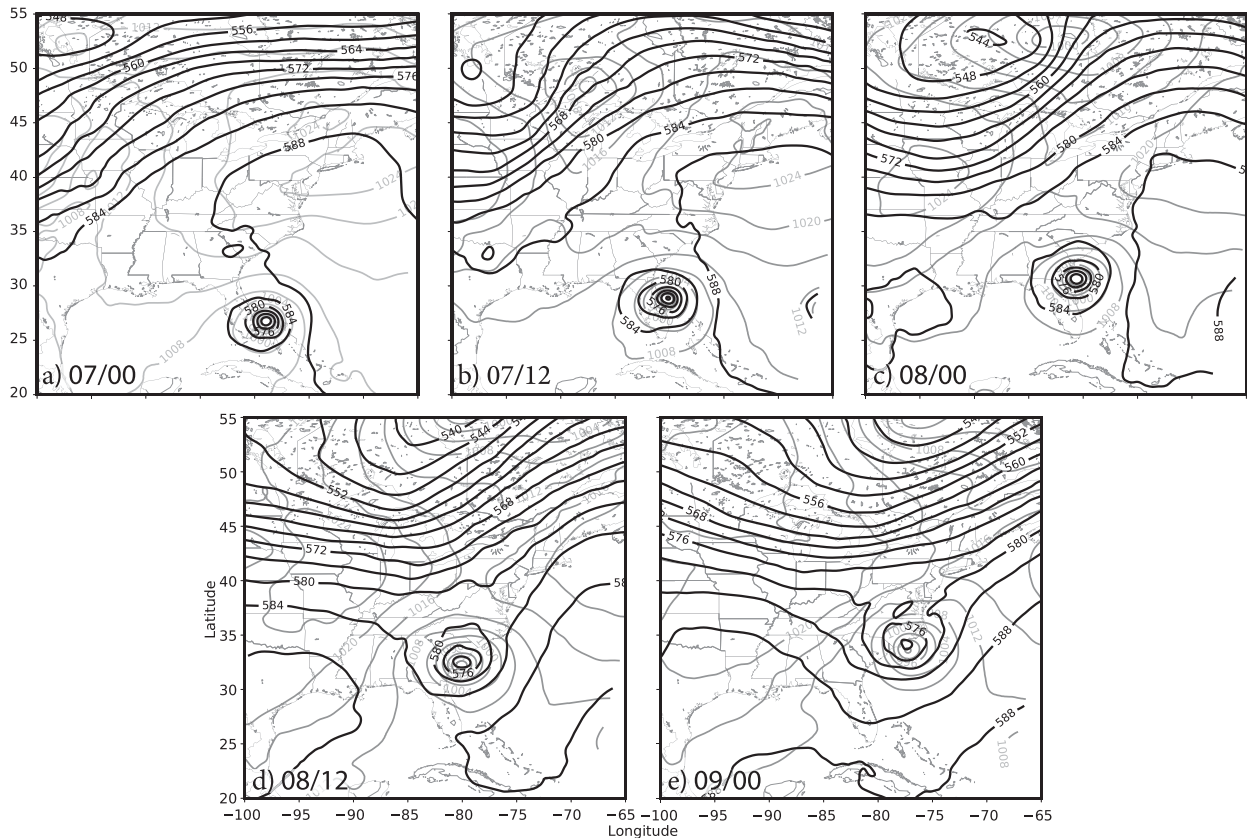
FIG. 3. 500-hPa geopotential height (dam; black contours) and mean sea level pressure (hPa; gray contours) over the eastern United States and western Atlantic from RAP analysis every 12 h from (a) 0000 UTC 7 Oct to (e) 0000 UTC 9 Oct.

(Bell and Bosart 1988; Lackmann and Stanton 2004; Rackley and Knox 2016). An objective algorithm for cold-air damming detection applied to mean sea level pressure estimates over the Carolinas and Virginia (Bailey et al. 2003) also indicates that weak cold-air damming took place between 0000 UTC 7 October and 0600 UTC 8 October. Mean sea level pressures from 0000 UTC 7 October to 0000 UTC 9 October at the stations shown in Fig. 2 are listed in Table 1. All conditions required by Bailey et al. (2003) for possible cold-air damming were met between 0000 UTC 7 October and 0600 UTC 8 October; however, we did not require the Laplacian of MSLP along each black segment in Fig. 2 to exceed any value. After 0600 UTC 8 October, MSLP in the central portions of VA, NC, and SC (respectively at LYH, GSO, and GSP) were continually less than MSLP farther inland (CRW, TRI, and TYS), meaning that cold-air damming was no longer occurring. Since almost all of the fronto-genesis occurred and precipitation fell after 0600 UTC 8 October over eastern NC and VA, cold-air damming did not significantly impact rainfall totals.

At 1200 UTC 8 October (Fig. 4g), a southwest–northeast-oriented frontal boundary extending from near the center of Matthew was apparent in eastern SC. At that time, the analyzed 950-hPa potential temperature near 36°N, 79°W (near Durham, NC) was 295–296 K, and near 34.5°N, 77.5°W (between Jacksonville and Wilmington, NC), it was 299–300 K. By 1800 UTC (Fig. 4h), a clear surface fron-tal boundary was present, and values of frontogenesis ex-ceeding $4.5 \, \text{K} \, 100 \, \text{km}^{-1} \, 3 \, \text{h}^{-1}$ existed along a narrow swath extending to southeastern VA. The temperature remained similar near the coast compared to at 1200 UTC but had dropped by about 1–3 K over central NC. The frontal boundary progressed northeastward with the maximum temperature gradient located near the coast of NC by 0000 UTC 9 October (Fig. 4i). Frontogenesis by that time exceeded $7.5 \, \text{K} \, 100 \, \text{km}^{-1} \, 3 \, \text{h}^{-1}$ along the entire front in NC and VA.

Figure 5a depicts estimated rainfall amounts over northeastern SC, eastern NC, and southern VA derived from radar and rain gauge[2] in the NCEP stage IV pre-cipitation dataset. Offshore data does not exist in this

---

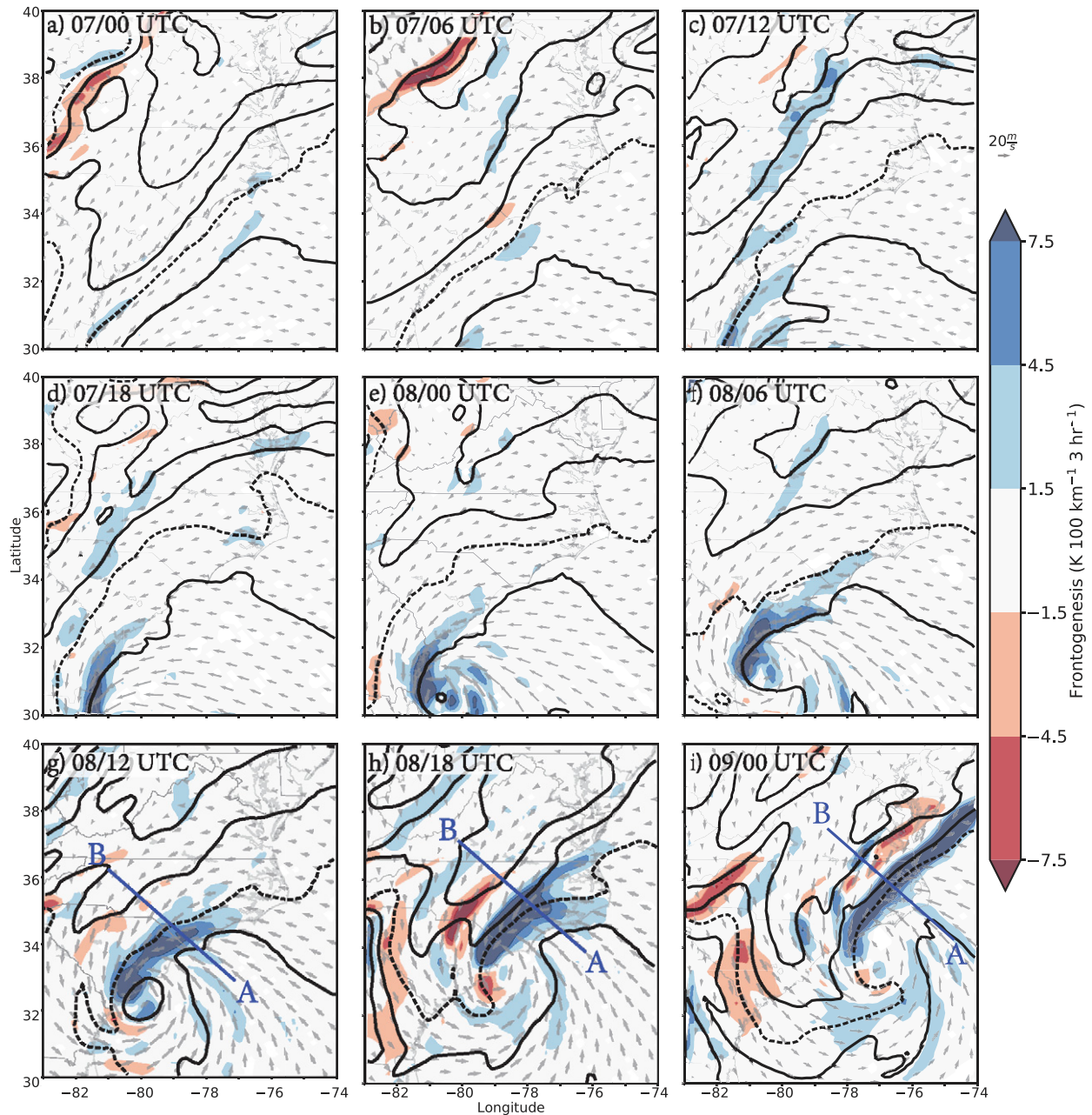[2] Estimates were obtained from the National Weather Service at http://water.weather.gov/precip/download.php.

FIG. 4. 950-hPa potential temperature (K; black contours with interval of 2 K), wind (vectors), and frontogenesis (K 100 km^{-1} 3 h^{-1}; shaded) from RAP analysis every 6 h over the southeastern United States from (a) 0000 UTC 7 Oct to (i) 0000 UTC 9 Oct. The dashed black line represents the 298-K potential temperature isotherm. In (g)–(i), solid blue lines and letters "A" and "B" denote cross sections illustrated by Fig. 8.

dataset. The largest rainfall amounts occurred inland along a swath located along a line from about 34°N, 79.5°W to 36°N, 78°W then east-northeastward toward southeastern Virginia near 37°N, 76°W. Some individual streaks of enhanced precipitation extended from southeast to northwest into and through the swath of highest amounts; as shown in section 4, these were likely associated with

convective cells that were focused along spiral rainbands that moved inland. Figure 5b shows the frequency of rainfall (defined by detection of >7 dBZ echo by WSR-88D) on 8–9 October. The greatest frequency of rainfall (60%+ of the time) included the region where the precipitation maximum was located but also extensive areas farther inland where smaller rainfall totals occurred. Thus, the

TABLE 1. Mean sea level pressure (hPa) at Automated Surface Observing Systems (ASOS) stations used for Bailey et al. (2003) cold-air damming detection algorithm.

Station/time	0000 UTC 7 Oct	0600 UTC 7 Oct	1200 UTC 7 Oct	1800 UTC 7 Oct	0000 UTC 8 Oct	0600 UTC 8 Oct	1200 UTC 8 Oct	1800 UTC 8 Oct	0000 UTC 9 Oct
CRW	1022.0	1020.3	1021.1	1019.3	1017.8	1016.6	1016.8	1017.3	1020.4
LYH	1024.6	1022.8	1022.0	1021.3	1019.3	1017.6	1015.9	1013.6	1013.3
ORF	1022.3	1021.0	1020.8	1020.0	1018.5	1016.2	1014.0	1009.3	1005.1
RIC	1024.3	1022.8	1022.5	1020.9	1019.7	1017.8	1015.9	1012.8	1011.6
TRI	1020.4	1018.7	1019.1	1017.0	1015.8	1013.8	1013.4	1012.2	1017.7
GSO	1022.0	1020.0	1018.9	1018.2	1016.2	1014.5	1011.4	1008.8	1009.4
ILM	1017.8	1016.1	1015.7	1014.7	1012.5	1009.4	1001.7	994.1	992.7
TYS	1018.5	1017.0	1019.0	1015.9	1014.8	1013.9	1013.9	1014.6	1018.3
GSP	1020.4	1018.6	1017.4	1016.2	1013.8	1011.7	1008.1	1007.9	1011.8
CHS	1016.7	1014.7	1012.7	1010.1	1004.5	995.8	984.1	996.2	1007.3

swath of large rainfall totals in eastern NC are present not simply because rainfall occurred for a longer time, but rather the precipitation there was more intense.

4. Radar echoes and frontogenesis over NC

Figure 6 shows observed reflectivity from WSR-88D at approximately 2.5 km above sea level every 3 h from 1200 UTC 8 October to 0300 UTC 9 October. The black contour outlines an area where F exceeded 1.5 K $100 \, \text{km}^{-1} \, 3 \, \text{h}^{-1}$ (blue shading in Fig. 4), and vectors indicate horizontal wind at 950 hPa. At 1200 UTC 8 October, a region of intense rainfall with reflectivity exceeding 35 dBZ was observed in southern NC and northeastern SC and was generally confined to regions close to where Matthew's spiral rainbands were located. The high reflectivity was mostly surrounded by the 1.5 K $100 \, \text{km}^{-1} \, 3 \, \text{h}^{-1}$ of F. Intense rainfall, while embedded within a broad stratiform region consisting of weaker rainfall, moved northeastward through NC over the next several hours. Generally, the most intense convective cells were located within discrete spiral tropical rainbands that were oriented from southeast to northwest.

As convective cells over the ocean moved inland, they typically became more intense, and by 1800 UTC, echoes with reflectivity exceeding 45 dBZ over eastern NC were not infrequent—particularly near 35.5°N, 78°W (Fig. 6c). By this time, intense 35+ dBZ echoes were not confined to inland spiral rainbands but were also found along and just inland of a developing frontal boundary (Fig. 4h) over eastern NC. By 2100 UTC, a principal spiral rainband extended inland from Cape Lookout (34.6°N, 76.5°W). Intense precipitation was then located well northeastward of the spiral rainbands along a line extending to the Chesapeake Bay from about 35.5°N, 78°W, or centered along the western edge of the 1.5 K $100 \, \text{km}^{-1}$ $3 \, \text{h}^{-1}$ F contour. The inland part of the spiral rainband intensified as it moved northeastward across eastern

and northeastern North Carolina by 0000–0300 UTC 9 October; some radar echoes then exceeded 50 dBZ over the coastal regions of northeastern NC and southeastern VA. Particularly over eastern NC, when comparing the distribution of rainfall (Fig. 5a) with radar echoes, the largest rainfall amounts appear to be oriented in streaks that probably correspond to the orientations of northeastward-moving rainbands when they were most intense. The spiral rainbands seen in Fig. 6 appear to have sometimes corresponded with locations of frontogenesis extending offshore.

Additionally, a secondary region of 35+ dBZ echoes developed over central NC and VA about 200 km inland from the region of primary frontogenesis around 1500 UTC and moved northeastward. At 1500 UTC, this area of heavy rainfall was centered near 36°N, 80.5°W (Fig. 6b), and a small region of F exceeding 1.5 K 100 km $3 \, \text{h}^{-1}$ existed in its vicinity through 0000 UTC, and is described in more detail below. The rainfall totals associated with this precipitation (Fig. 5a) were not as large as those along the near-surface front associated with the great rain totals, but the period of heavy rain farther inland than the main front probably also contributed to high river levels on the coastal plain in the days following Matthew.

Figure 7, which is similar to Fig. 4, provides a magnified view of 950 hPa F, θ (with 1-K contours), and wind at higher temporal resolution. The inland part of the principal spiral rainband seen in Fig. 6 was located near confluent low-level flow, and the largest values of F corresponded to areas of maximum confluence. At 1200–1800 UTC, the axis of confluence along which frontogenesis occurred became more zonally oriented with increasing latitude. For example, at 1800 UTC (Fig. 7c), maximum F was generally oriented from southwest to northeast south of 35°N. North of 35°N, two separate areas of large F were present. One continued northeastward into far southeastern VA. The other extended toward the east to about 76°W. By 0000 UTC,
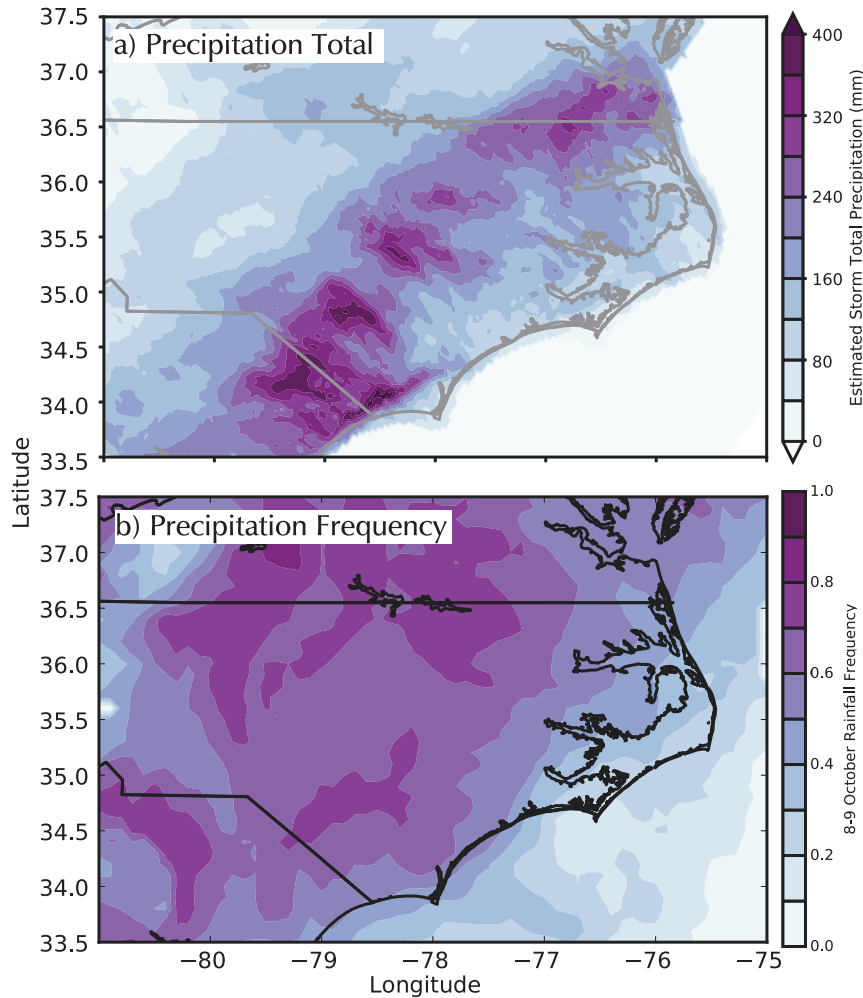
FIG. 5. (a) Estimated total precipitation on 8–9 Oct derived from radar and rain gauge data using the NCEP stage IV precipitation dataset. (b) Fraction of time on 8–9 Oct during which rain detected by radar occurred.

the axis of maximum F was contained within a single long region extending from southwest to northeast throughout eastern NC, VA, and offshore (Fig. 4i). Where the axis of confluent flow was oriented from southwest to northeast, $\sim$15–20 m s^{-1} northeasterly wind was situated between stronger easterly, warm, and moist wind to its east and north-northeasterly, colder, and drier flow to its west. The zonally oriented frontogenesis (that along 35°N at 1800 UTC) was weaker than frontogenesis farther inland, but it apparently contributed to tightening the temperature gradient over eastern NC before air there was advected toward the front. For example, near 35°N, 77°W (inland from the Pamlico Sound), the 298- and 299-K θ contours were separated meridionally along 77°W by approximately 74 km at 1200 UTC. Frontogenesis occurred between 1500 and 1800 UTC, and by 1800 UTC, the two contours were separated meridionally by only 42 km.

During the entire time period displayed in Fig. 7, the temperature gradient along the near-surface front mostly increased to the west of the 298-K contour, which is where most of the 35+ dBZ echo was located. Another secondary region of low-level frontogenesis was also present to the northwest and west of the near-surface front. It was located near 78°W somewhere between 35.5°N and north of 37.5°N at 1500, 2100, and 0000 UTC, or in the vicinity of the secondary region of 35+ dBZ echo that was located over central NC and VA and described above (Figs. 6b–d). Magnitudes of F in this region exceeded 7.5 K 100 km^{-1} 3 h^{-1} at 2100 and 0000 UTC. By 0300 UTC, the temperature gradient formed by this secondary area of low-level frontogenesis had merged with the near-surface front near the coasts of NC and VA. The increasing temperature gradient along the near-surface front probably aided development of 45+ dBZ radar echoes along the
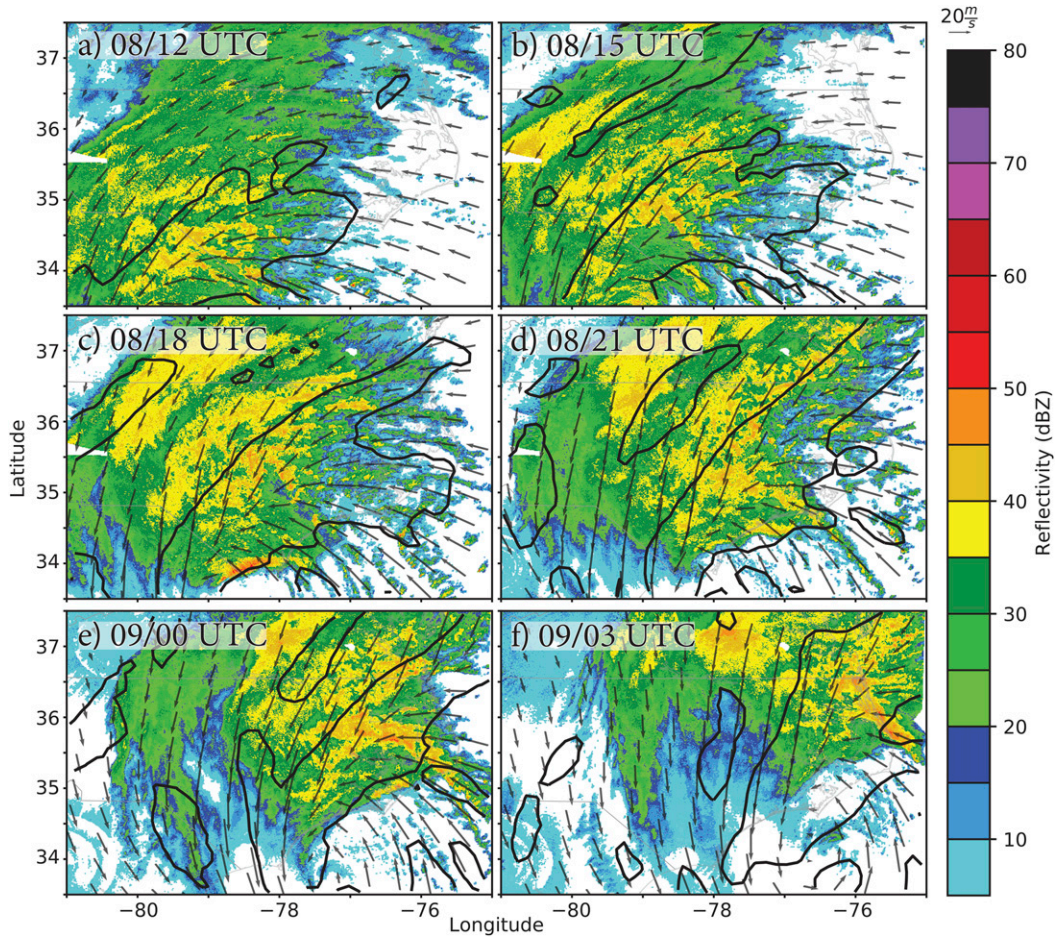
FIG. 6. Observed radar reflectivity (dBZ; shaded) from WSR-88D at 2.5 km above sea level and 950-hPa wind (vectors) every 3 h from (a) 1200 UTC 8 Oct to (f) 0300 UTC 9 Oct. The black contour outlines 950-hPa frontogenesis greater than 1.5 K 100 km^{-1} 3 h^{-1}.

principal spiral rainband after 1800 UTC in northeastern NC and southeastern VA.

Figure 8 includes three representative cross sections of moisture convergence (g kg^{-1} h^{-1}; shading), saturated equivalent potential temperature θ_{es} (contours with interval of 2 K), and wind (vectors)—at 1200 and 1800 UTC 8 October and at 0000 UTC 9 October. Moisture convergence is defined as

$$q_{conv} = -\mathbf{V}_h \cdot \nabla q, \tag{3}$$

in which $\mathbf{V}_h$ is the horizontal wind, and q is specific humidity. Analyzed vertical wind is multiplied by 10 for display purposes. The 332-K contour is red. The right side of the abscissas in Fig. 8 correspond to point A at the southeast end of the blue lines drawn in Figs. 4g–i. Point B in Figs. 4g–i is located at the other end of each cross section, 500 km to the northwest of point A. The cross sections were selected so that they were approximately

normal to the temperature gradient along the near-surface front and located near the heaviest rainfall in the principal spiral rainband. Conditionally, symmetrically unstable areas are represented by black dots, which are mostly seen below 500 hPa between 300 and 500 km from point A.

All cross sections contained a maximum in q_{conv} exceeding 18 g kg^{-1} h^{-1} between 1000 and 900 hPa. The maximum in q_{conv} tilted northwestward with height behind the surface front, and q_{conv} of 6–12 g kg^{-1} h^{-1} was present between 600 and 700 hPa in each cross section. To the southeast of the maximum boundary layer q_{conv}, θ_{es} isotherms below 900 hPa tilted sharply toward the southeast with height in warm, moist air. To the northwest of the maximum boundary layer q_{conv}, isotherms of θ_{es} tilted southeastward with height up to about 950 hPa and then generally northwestward with height above 950 hPa. However, at 1200 UTC 8 October, the 334- and 336-K θ_{es} contours tilted southeastward with height
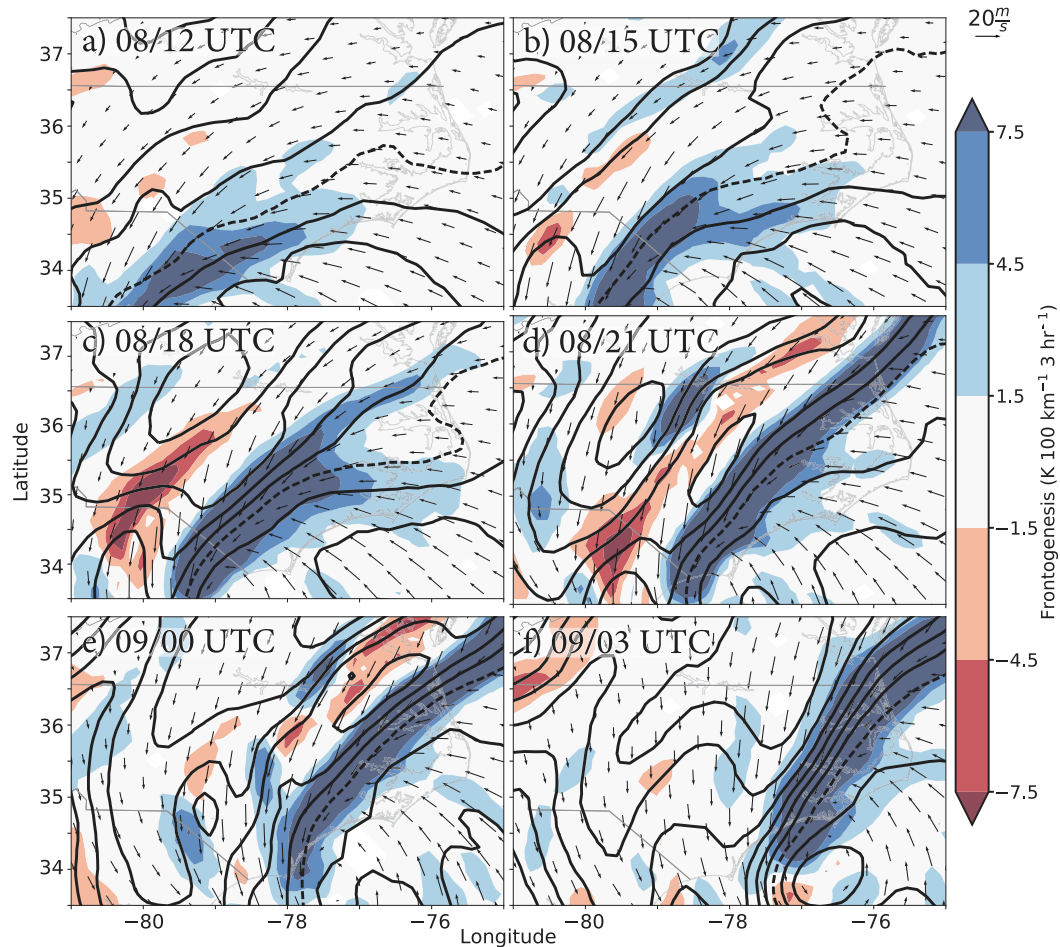
FIG. 7. As in Fig. 4, but zoomed in over eastern North Carolina and displayed every 3 h from (a) 1200 UTC 8 Oct to (f) 0300 UTC 9 Oct. Potential temperature contour interval is 1 K.

between 700 and 500 hPa around a θ_{es} minimum at 500 hPa. Also, at 0000 UTC 9 October, the 330–334-K isotherms tilted southeastward with height to 950 hPa and then sharply toward the northwest around 900 hPa. About 425 km northwest of point A, the isotherms tilted back toward the southeast up to about 600 hPa as they wrapped around a θ_{es} maximum around 800 hPa about 375 km from point A. The θ_{es} isotherms then tilted back toward the northwest around a θ_{es} minimum in conditionally symmetrically unstable air above 600 hPa near point B, which was located within the secondary area of the 35+ dBZ echo over central VA (Fig. 6e).

Comparison of the three panels in Fig. 8 also reveals the production of a near-surface temperature gradient near and immediately west of the area of maximum moisture convergence. At 1000 hPa, the distance between the 332- and the 342-K θ_{es} contours shrunk from 165 km at 1200 UTC to 45 km at 1800 UTC, and 44 km by 0000 UTC. Below 900 hPa, the 342-K contour was always located near the location of maximum q_{conv}.

Contours of lower θ_{es} moved eastward relative to maximum q_{conv}, consistent with the evolution of temperature gradients illustrated in Figs. 4 and 7. Figure 8c also shows the two near-surface regions with a large temperature gradient seen in Fig. 7e: the primary front between 200 and 300 km from point A, and a second smaller gradient another ~100 km to the northwest.

5. Atmospheric instability

Colle (2003) described how the release of conditional symmetric instability may have intensified rainfall over the northeastern United States during Hurricane Floyd (section 1). How conditional symmetric instability should be calculated remains an unsettled question. Schultz and Schumacher (1999) used the geostrophic wind to compute moist geostrophic PV, $\mathcal{P}_g$, which is defined as

$$\mathcal{P}_g = g\boldsymbol{\eta}_g \cdot \nabla\theta_{es}, \qquad (4)$$
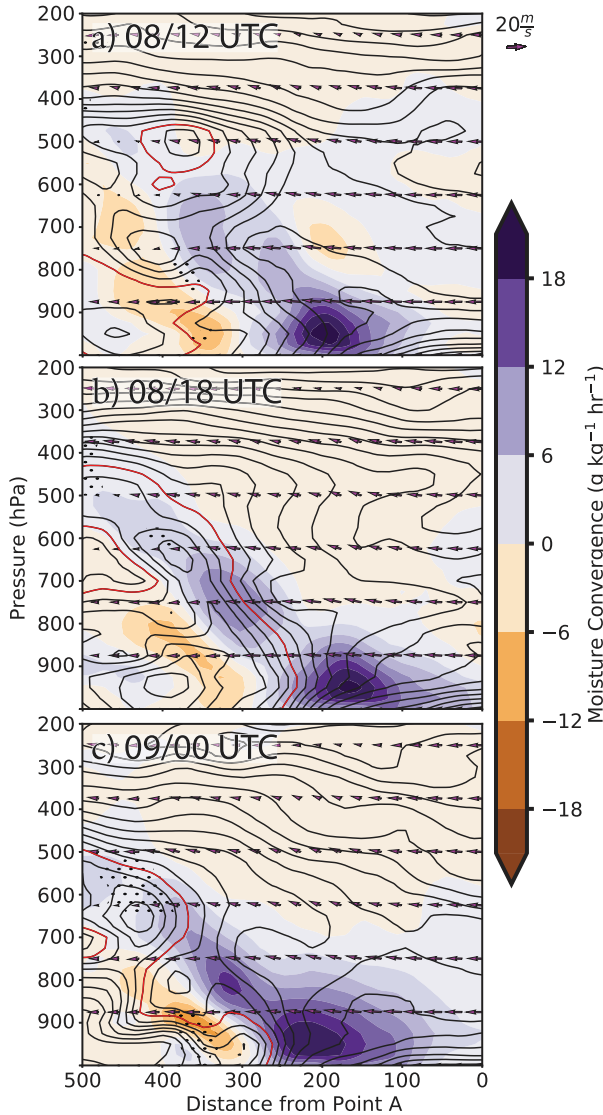
FIG. 8. Southeast–northwest cross sections of moisture convergence (g kg^{-1} h^{-1}; shaded), wind along the cross section with vertical velocity multiplied by 10 (vectors), and saturated equivalent potential temperature (K; contours with interval of 2 K) every 6 h from (a) 1200 UTC 8 Oct to (c) 0000 UTC 9 Oct. The red contour denotes the 332-K isotherm. The cross sections correspond to those drawn in Figs. 4g–i. In each panel, point A is on the right side of the abscissa. Black dots indicate areas of conditional symmetric instability.

in which the variable $g = 9.81$ m s^{-1}, $\boldsymbol{\eta}$ is the full three-dimensional vorticity, θ_{es} is the saturated equivalent potential temperature, and subscript g represents the geostrophic part of the subscripted variable.

Others (Gray and Thorpe 2001; Clark et al. 2002; Jurewicz and Evans 2004; Novak et al. 2004, 2006; Schultz and Knox 2007) used the total wind to calculate the moist PV, $\mathcal{P}$, which is defined similarly to $\mathcal{P}_g$, except that the total wind is included:

$$\mathcal{P} = g\boldsymbol{\eta} \cdot \nabla\theta_{es}. \tag{5}$$

Alternatively, the balanced flow—in this case, the nondivergent flow—could be substituted for use in Eq. (5) (Nielsen-Gammon and Gold 2008). Depending on the method utilized, conditional symmetric instability is present when $\mathcal{P}$ is negative or slightly positive and the atmosphere is not conditionally or inertially unstable (Novak et al. 2006). We used both the total wind and nondivergent wind and found only minor differences in calculation of $\mathcal{P}$. Only results using the total wind are displayed herein. We have also checked that the vertical component of $\boldsymbol{\eta}$ is much larger than the horizontal components; therefore, for our purposes, $\boldsymbol{\eta}$ in Eq. (5) can be readily approximated here as $\zeta + f$, in which $f = 2\Omega\sin(\varphi)$ is the Coriolis parameter, and the gradient of θ_{es} can be taken on isobaric surfaces. The variable ζ is the relative vorticity, such that

$$\zeta = \frac{\partial v}{\partial x} - \frac{\partial u}{\partial y}. \tag{6}$$

Then, $\mathcal{P}$ takes the form of Ertel PV (a negative sign is introduced since the gradient of θ_{es} is taken along the pressure coordinate now), except here we have the moist Ertel PV:

$$\mathcal{P} \approx -g(\zeta + f)\frac{\partial\theta_{es}}{\partial p}. \tag{7}$$

Thus, $\mathcal{P}$ is negative when $\zeta + f$ and $\partial\theta_{es}/\partial p$ is of the same sign, and herein, we assert that conditional symmetric instability was present during Matthew if $\mathcal{P}$ was negative and $\partial\theta_{es}/\partial p < 0$. Air was conditionally unstable where $\mathcal{P}$ was positive and $\partial\theta_{es}/\partial p < 0$.

Figure 9 depicts the instability of air at 925 hPa (shading) at 3-hourly intervals between 1200 UTC 8 October and 0300 UTC 9 October. Areas where 35+ dBZ radar echoes were present at 2.5-km altitude are outlined by black contours. In this figure, the reflectivity field was degraded to 0.1° grid spacing. Vectors denote 925-hPa winds. Blue and green shading indicate conditional and conditional symmetric instability, respectively. Air over the ocean or coastal regions of SC, NC, or VA was apparently never conditionally symmetrically unstable. Instead, the low-level warm, oceanic air flowing into the region of frontogenesis from the east and southeast was all conditionally unstable. Before 9 October, no low-level conditional symmetric instability was present within or upstream of the 35+ dBZ echo region except over a small area on the southernmost, downstream edge of the 35+ dBZ echoes between 79° and 80°W. However, at 0000 UTC, a corridor of conditional symmetric instability extending from about
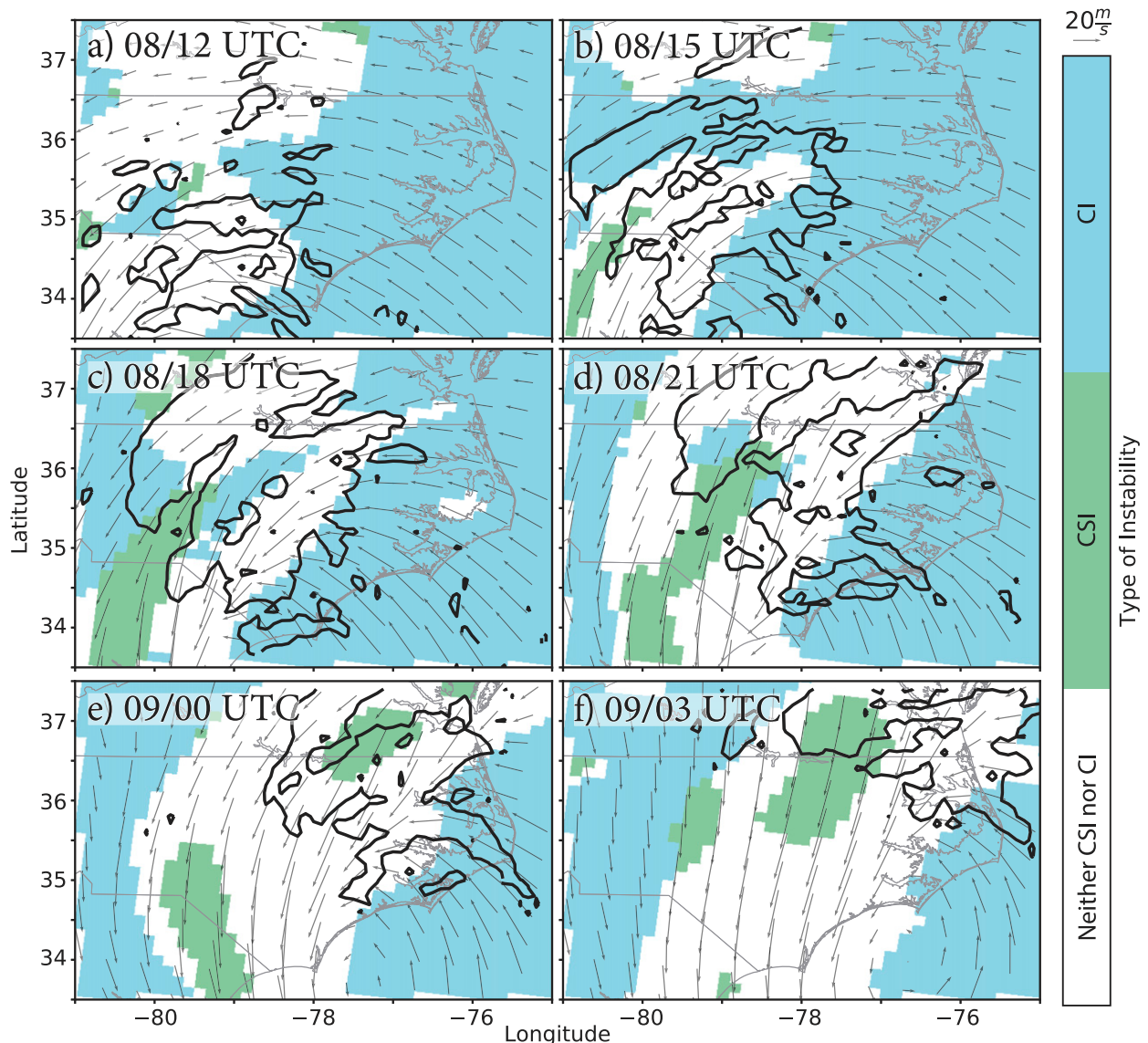
FIG. 9. Maps of atmospheric instability at 925 hPa from (a) 1200 UTC 8 Oct to (f) 0300 UTC 9 Oct. Blue indicates conditional instability, green represents conditional symmetric instability, and white denotes neither conditional nor conditional symmetric instability. 925-hPa wind vectors are displayed. The black contour outlines 35 dBZ radar reflectivity after WSR-88D is interpolated to a 0.1° grid.

36.75°N, 77.25°W to near 38.5°N, 75°W (Fig. 10) may have enhanced rainfall intensity in the 35+ dBZ echo located southwest or south (i.e., downstream) of the instability. By 0300 UTC, only the area of conditional symmetric instability seen in Fig. 9f remained. Analysis of midlevel (500–700 hPa) instability (not shown) indicates that conditional symmetric instability was also present near or within the secondary 35+ dBZ echo region located over central NC and VA (around 37°N, 78°W at 0000 UTC) after 1800 UTC 8 October. This instability was located in a region of midlevel moisture convergence approximately 200 km behind the near-surface front (Fig. 8c). Unsurprisingly, most of the

low-level air within the 35+ dBZ echo region was neither conditionally unstable nor conditionally symmetrically unstable.

6. Conclusions

In October 2016, Hurricane Matthew generated extreme rainfall during its extratropical transition, in some places exceeding 400 mm total, over a swath that extended from eastern South Carolina (SC) through eastern North Carolina (NC) and southeastern Virginia (VA). Synoptic-scale conditions were favorable (Fig. 3) for the observed left-of-track precipitation distribution
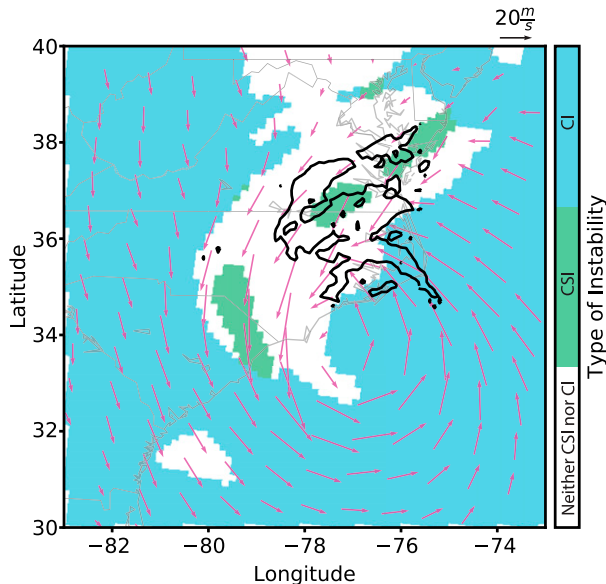
FIG. 10. As in Fig. 9e, but for a larger area spanning 30°–40°N, 73°–83°W.

that has been well documented by prior studies (section 1) of tropical cyclones undergoing extratropical transition along the U.S. East Coast.

Cold-air damming occurred over North Carolina as late as 0600 UTC 8 October (section 3); however, sustained frontogenesis did not begin where the heaviest rainfall occurred until about 1200 UTC (Figs. 4, 7). Therefore, we conclude that, although weak cold-air damming probably occurred prior to Matthew reaching NC, cold-air damming did not impact precipitation totals in NC and VA during Matthew. This conclusion corroborates that of Garcia-Rivera et al. (2016), who studied rainfall patterns over NC during the weaker Tropical Storm Kyle from 2002.

As Matthew moved northeastward along the NC and SC coastlines, a near-surface front developed about 100–200 km inland (Figs. 4, 7), and the corridor of heaviest precipitation corresponded closely in space to the location of the front (Figs. 5, 6). The largest rainfall totals at a given time during Matthew generally occurred at locations where the spiral rainband(s) intersected the frontal boundary, which was approximately normally oriented relative to the spiral rainbands. The northeastward-moving spiral rainbands occurred in areas of large moisture convergence and consisted of discrete oceanic cells that moved inland (counterclockwise around Matthew) then merged into a larger contiguous region of intense convection as the cells approached the surface front. The banded distribution pattern of total rainfall exhibited in Fig. 5a was probably associated with fluctuations in the intensity of rainfall in the principal spiral rainband as it moved northeastward.

In contrast to the simulation of Hurricane Floyd by Colle (2003), we found no evidence of conditional symmetric instability to the east of the near-surface front over eastern SC, NC, and VA. Instead, within and outside of the spiral rainbands, low-tropospheric flow advected warm, moist, conditionally unstable air from the ocean toward the front, which promoted the lift of the air 100–200 km inland from the coast in NC. Not all of the rainfall in the swath of largest precipitation totals fell within a spiral rainband. A radar echo with reflectivity ≥35 dBZ also developed north of the principal spiral rainband along the western edge of the southwest–northeast-oriented axis of near-surface frontogenesis (Figs. 6b–e). A secondary region of frontogenesis farther inland near the NC–VA border at 78°W appeared to be related to an intense radar echo that developed over central NC and VA after 1200 UTC 8 October (Figs. 6, 7). Release of midlevel (between 400 and 600 hPa) conditional symmetric instability may have partially enhanced rainfall there (Figs. 8b,c). After 0000 UTC 9 October, the inland temperature gradient merged with the coastal front (Figs. 7h–i), thereby increasing the temperature gradient at the coast by 0300 UTC. This coincided with invigoration of precipitation in the spiral rainband over NC and VA at that time (Fig. 6f).

Not detailed in this study are the polarimetric and three-dimensional characteristics of radar echoes within Matthew. We noted during the course of our study that the polarimetric signature of discrete convective radar echoes embedded within spiral rainbands evolved as they moved closer to shore. While we have not investigated this phenomenon in great detail, we speculate that different aerosol composition or concentration over the ocean and land may explain our observation. Also of particular interest to the authors are the kinematics of a near-coastal band of extreme rainfall (Fig. 6c) that persisted just along the North Carolina coast on 8 October. Although the precipitation distribution of Matthew was generated by mechanisms similar to that of other cyclones undergoing extratropical transition, the unique track of Matthew's center parallel to but just offshore the U.S. East Coast provides previously unavailable opportunities to utilize dual-polarimetric WSR-88D data and explore the evolution of convection over several days as the hurricane weakened and transitioned into a post-tropical cyclone.

REFERENCES

Atallah, E. H., and L. F. Bosart, 2003: The extratropical transition and precipitation distribution of Hurricane Floyd (1999). *Mon. Wea. Rev.*, **131**, 1063–1081, https://doi.org/10.1175/1520-0493(2003)131<1063:TETAPD>2.0.CO;2.

——, ——, and A. R. Aiyyer, 2007: Precipitation distribution associated with landfalling tropical cyclones over the eastern United States. *Mon. Wea. Rev.*, **135**, 2185–2206, https://doi.org/10.1175/MWR3382.1.

Bailey, C. M., G. Hartfield, G. M. Lackmann, K. Keeter, and S. Sharp, 2003: An objective climatology, classification scheme, and assessment of sensible weather impacts for Appalachian cold-air damming. *Wea. Forecasting*, **18**, 641–661, https://doi.org/10.1175/1520-0434(2003)018<0641:AOCCSA>2.0.CO;2.

Bell, G. D., and L. F. Bosart, 1988: Appalachian cold-air damming. *Mon. Wea. Rev.*, **116**, 137–161, https://doi.org/10.1175/1520-0493(1988)116<0137:ACAD>2.0.CO;2.

Benjamin, S. G., and Coauthors, 2016: A North American hourly assimilation and model forecast cycle: The Rapid Refresh. *Mon. Wea. Rev.*, **144**, 1669–1694, https://doi.org/10.1175/MWR-D-15-0242.1.

Bosart, L. F., and D. B. Dean, 1991: The Agnes rainstorm of June 1972: Surface feature evolution culminating in inland storm redevelopment. *Wea. Forecasting*, **6**, 515–537, https://doi.org/10.1175/1520-0434(1991)006<0515:TAROJS>2.0.CO;2.

Clark, J. H. E., R. P. James, and R. H. Grumm, 2002: A reexamination of the mechanisms responsible for banded precipitation. *Mon. Wea. Rev.*, **130**, 3074–3086, https://doi.org/10.1175/1520-0493(2002)130<3074:AROTMR>2.0.CO;2.

Colle, B. A., 2003: Numerical simulations of the extratropical transition of Floyd (1999): Structural evolution and responsible mechanisms for the heavy rainfall over the northeast United States. *Mon. Wea. Rev.*, **131**, 2905–2926, https://doi.org/10.1175/1520-0493(2003)131<2905:NSOTET>2.0.CO;2.

Croke, M. S., 2005: Examining planetary, synoptic, and mesoscale features that enhance precipitation associated with landfalling tropical cyclones in North Carolina. M.S. thesis, Dept. of Marine Earth and Atmospheric Sciences, North Carolina State University, 231 pp.

Evans, C., and Coauthors, 2017: The extratropical transition of tropical cyclones. Part I: Cyclone evolution and direct impacts. *Mon. Wea. Rev.*, **145**, 4317–4344, https://doi.org/10.1175/MWR-D-17-0027.1.

Garcia-Rivera, J. M., Y.-L. Lin, and Y. Rastigejev, 2016: Tropical Storm Kyle (2002) and cold-air damming: Their interactions and impacts on heavy rainfall in the Carolinas. *Meteor. Atmos. Phys.*, **128**, 347–372, https://doi.org/10.1007/s00703-015-0421-1.

Gray, S. L., and A. J. Thorpe, 2001: Parcel theory in three dimensions and the calculation of SCAPE. *Mon. Wea. Rev.*, **129**, 1656–1672, https://doi.org/10.1175/1520-0493(2001)129<1656:PTITDA>2.0.CO;2.

Jones, S. C., and Coauthors, 2003: The extratropical transition of tropical cyclones: Forecast challenges, current understanding, and future directions. *Wea. Forecasting*, **18**, 1052–1092, https://doi.org/10.1175/1520-0434(2003)018<1052:TETOTC>2.0.CO;2.

Jurewicz, M. L., Sr., and M. S. Evans, 2004: A comparison of two banded, heavy snowstorms with very different synoptic settings. *Wea. Forecasting*, **19**, 1011–1028, https://doi.org/10.1175/WAF-823.1.

Lackmann, G. M., and W. M. Stanton, 2004: Cold-air damming: Physical mechanisms, synoptic settings, and model representation. Preprints, *20th Conf. on Weather Analysis and Forecasting/16th Conf. on Numerical Weather Prediction*, Seattle, WA, Amer. Meteor. Soc., 18.6, https://ams.confex.com/ams/84Annual/techprogram/paper_73411.htm.

Nielsen-Gammon, J. W., and D. A. Gold, 2008: Dynamical diagnosis: A comparison of quasigeostrophy and Ertel potential vorticity. *Synoptic-Dynamic Meteorology and Weather Analysis and Forecasting, Meteor. Monogr.*, No. 33, Amer. Meteor. Soc., 183–202.

NOAA, 2018a: Surface analysis 21Z Sat Oct 8 2016. NOAA, accessed 26 November 2018, https://www.wpc.ncep.noaa.gov/html/sfc-zoom.php?h=21&y=2016&m=10&d=08.

——, 2018b: WPC QPF Archive. NOAA, accessed 26 November 2018, https://www.wpc.ncep.noaa.gov/archives/qpf/get_qpf_images.php.

Novak, D. R., L. F. Bosart, D. Keyser, and J. S. Waldstreicher, 2004: An observational study of cold season-banded precipitation in northeast U.S. cyclones. *Wea. Forecasting*, **19**, 993–1010, https://doi.org/10.1175/815.1.

——, J. S. Waldstreicher, D. Keyser, and L. F. Bosart, 2006: A forecast strategy for anticipating cold season mesoscale band formation within eastern U.S. cyclones. *Wea. Forecasting*, **21**, 3–23, https://doi.org/10.1175/WAF907.1.

Petterssen, S., 1936: Contribution to the theory of frontogenesis. *Geofys. Publ.*, **11** (6), 1–27.

Rackley, J. A., and J. A. Knox, 2016: A climatology of southern Appalachian cold-air damming. *Wea. Forecasting*, **31**, 419–432, https://doi.org/10.1175/WAF-D-15-0049.1.

Schultz, D. M., and J. A. Knox, 2007: Banded convection caused by frontogenesis in a conditionally, symmetrically, and inertially unstable environment. *Mon. Wea. Rev.*, **135**, 2095–2110, https://doi.org/10.1175/MWR3400.1.

——, and P. N. Schumacher, 1999: The use and misuse of conditional symmetric instability. *Mon. Wea. Rev.*, **127**, 2709–2732. *Corrigendum*, **128**, 1573.

Stewart, S. R., 2017: Tropical Cyclone Report: Hurricane Matthew (28 September–9 October 2016). NHC Rep. AL142016, NOAA/NWS/NCEP/National Hurricane Center, 96 pp., https://www.nhc.noaa.gov/data/tcr/AL142016_Matthew.pdf.